Impedance Spectroscopic Analysis of Lead Iodide Perovskite-Sensitized Solid-State Solar Cells

Amalie Dualeh, Thomas Moehl,* Nicolas Tétreault, Joël Teuscher, Peng Gao, Mohammad Khaja Nazeeruddin, and Michael Grätzel*

Institute of Chemical Sciences and Engineering, Laboratory of Photonics and Interfaces, École Polytechnique Fédérale de Lausanne, Lausanne, Switzerland

ABSTRACT Mesoscopic solid-state solar cells based on the inorganic–organic hybrid perovskite $CH_3NH_3PbI_3$ in conjunction with the amorphous organic semiconductor spiro-MeOTAD as a hole transport material (HTM) are investigated using impedance spectroscopy (IS). A model to interpret the frequency response of these devices is established by expanding and elaborating on the existing models used for the liquid and solid-state dye-sensitized solar cells. Furthermore, the influence of changing the additive concentrations of *tert*-butylpyridine and LiTFSI in the HTM and varying the HTM overlayer thickness on top of the sub-micrometer thick TiO_2 on the extracted IS parameters is investigated. The internal electrical processes of such devices are studied and correlated with the overall device performance. In particular, the features in the IS responses that are attributed to the ionic and electronic transport properties of the perovskite material and manifest as a slow response at low frequency and an additional RC element at intermediate frequency, respectively, are explored.

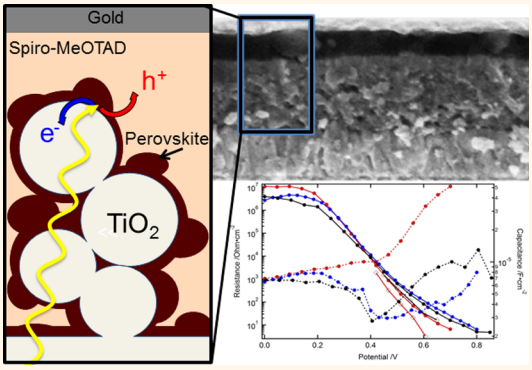

KEYWORDS: mesoscopic solar cells · perovskite · impedance spectroscopy · spiro-MeOTAD · *tert*-butylpyridine · LiTFSI

The growing demand for renewable energy sources has led to considerable development in many areas related to the research and manufacture of solar cells. In an effort to generate more cost-effective technology, the field of thin film solar photovoltaics presents a promising avenue toward high efficiency solar energy conversion.

The third generation solar cells combine diverse concepts and materials for the efficient harvest of sunlight. Purely organic devices as well as the electrochemical solar cells (*i.e.*, dye-sensitized solar cells, DSCs) and quantum dot solar cells with their solid-state counterparts show promising results and are partly already in the first stages of emerging into the market. Though these types of solar cells are diverse in materials and design, they have one idea in common. They all possess a high extinction coefficient absorber (molecular quantum dot or a thin absorber layer) at a heterointerface. Normally, the heterointerface has a high surface area to increase absorption while maintaining a thin absorber layer.

With the publication by Im *et al.*[1] in 2011, the research of lead-based perovskites as potential high extinction light absorbers in solar cells intensified, while Chung *et al.*[2] demonstrated, in addition to the light-absorbing properties, the hole transport capabilities of a closely related perovskite material. The subsequent publications of Kim *et al.*[3] and Lee *et al.*[4] in 2012 reported high efficiency solid-state devices using the lead halide perovskite system on conductive and insulating mesoporous substrates.

Important to note here is the uniqueness of the mixed-halide perovskite utilized by Lee *et al.*[4] and Ball *et al.*[5] In this case, perovskite is deposited from a mixture in dimethylformamide-containing $PbCl_2$ and CH_3NH_3I and was shown to behave as both electron and hole transport material. As is seen from the work presented by Ball *et al.*,[5] the perovskite forms a compact overlayer on top of the mesoporous metal oxide scaffold of approximately 250 nm.

The system investigated here uses a similar lead-iodide-based perovskite as

* Address correspondence to michael.graetzel@epfl.ch, thomas.moehl@epfl.ch.

Received for review August 19, 2013 and accepted December 16, 2013.

Published online December 16, 2013
10.1021/nn404323g

light-absorbing material in a solid-state mesoscopic heterojunction style solar cell employing the amorphous organic p-type semiconductor 2,2′,7,7′-tetrakis-(*N*,*N*-di-*p*-methoxyphenylamine)-9,9′-spirobifluorene (spiro-MeOTAD) as the hole transport material (HTM). The lead iodide perovskite in this work is deposited by spin-coating from a 1:1 molar ratio solution of PbI_2 and CH_3NH_3I in γ-butyrolactone (GBL) directly onto the mesoporous TiO_2 films following the procedure reported by Kim *et al.*[3] These films are subsequently annealed at 100 °C for 10 min, leading to the formation of the inorganic–organic lead-iodide-based perovskite, $CH_3NH_3PbI_3$ crystallites.

While Lee *et al.*[4] showed that a mixed-halide perovskite on a mesoporous Al_2O_3 photoanode acts as both light absorber and electron conductor, Etgar *et al.*[6] showed that the pure iodide perovskite can act as a hole conductor. Similar to Etgar *et al.*, Chung *et al.*[2] showed that a similar perovskite material, $CsSnI_3$, functions as a hole conductor.

This demonstrates the intriguing property of perovskites in that they do not only act as light absorbers but participate in the charge conduction. Furthermore, the perovskite halides do not only possess electronic charge conduction but might additionally exhibit ionic charge conduction. Ionic conduction has been reported for perovskite-type halides such as $CsPbCl_3$.[7] In the case of a perovskite-type oxide $La_{2/3}TiO_3$, lithium ion conduction has been observed when lithium is partially substituted for Lanthanum, and the measured conductivity was one of the highest for lithium ion conductors chemically stable at ambient atmospheric conditions.[8] In this structure, 1/3 of the A sites of the perovskite structure are vacant, allowing the Li ions (which are substituted for La in A sites) to move through the vacancies.

The ease with which these inorganic–organic hybrid perovskite materials can be prepared and processed from solution[9,10] while simultaneously providing desired device characteristics has made them an attractive alternative in the field of electronics. The relationship between the organic and the inorganic components and its impact on the material structure and properties can be exploited to design and develop materials for targeted applications.[11–13] Generally, the relatively simple organic component in these hybrid structures has been found to play a secondary role in determining the physical properties and serve more to define the crystal structure of the material. This is the case for the conducting tin(II)-halide-based perovskite where the high conductivity arises due to the high mobility of the tin iodide sheets while the organic component defines the structure.[14] Alternatively, the use of oligothiophene chromophores as the organic component in combination with lead(II) halide layers allowed charge transfer between the separate components and thus not only defined the dimensionality of the lead(II) halide layers but also determined the photoluminescent properties of the material.[12] Chang *et al.*[15] not only examined the electronic and structural properties of the lead-halide-based inorganic–organic perovskite $CH_3NH_3PbX_3$ (X = Cl, Br, I) but also determined that the physical coupling between the organic and inorganic components is weak, allowing easy rotation of the organic CH_3NH_3 constituent.

A further advantage of these materials is the relative ease with which their light-harvesting capabilities can be tuned by chemical management as shown by Noh *et al.*[16] This further allows more freedom and improved matching between the perovskite and the HTM used.[17–19]

In order to correctly identify the role of the individual components and their contribution to the device performance of working solar cells, several different systems were investigated in addition to the complete working perovskite-based devices. In general, it has to be shown to what extent the behavior of the perovskite devices shares properties with the known liquid and solid-state DSC device types and therefore to what extent the equivalent circuits of these known devices can be applied to the analysis of the perovskite-based devices. For this reason, we have investigated several example systems and compared them to the perovskite devices, which included the liquid and solid-state DSC type as well as the influence of the variation of the lithium bis(trifluoromethanesulfonyl)imide (LiTFSI) salt and *tert*-butylpyridine (TBP) concentration in the HTM solution and the spiro-MeOTAD overlayer thickness on top of the sensitized mesoporous TiO_2.

RESULTS AND DISCUSSION

Considerations of the System under Investigation and Impedance Spectroscopy Measurement. The system under consideration in this work shares similarities with the well-known liquid electrolyte-based dye-sensitized solar cell (DSC). A DSC uses a dye as light absorber which is adsorbed on a mesoporous TiO_2 ($mTiO_2$). The electron from the light-excited dye is injected into the $mTiO_2$, transported to the back contact of the photoanode, and collected. At the counter electrode, the electron is then used to regenerate a redox system in a liquid electrolyte and the reduced form of the redox system is transported through the electrolyte media to the photoanode and regenerates the oxidized dye. A closely related device type to the DSC is a solid-state DSC (ssDSC) in which the liquid electrolyte component is replaced by an organic hole conductor, normally spiro-MeOTAD. In the case of ssDSCs, the $mTiO_2$ thickness is limited by the pore infiltration of the organic HTM and its short diffusion length of charge carriers. Hence, ssDSCs generally use thinner $mTiO_2$ films of 2–3 μm compared with the liquid-state alternative, which use up to 15 or even 20 μm. The perovskite-based solar cells in this work use $CH_3NH_3PbI_3$ in place of the dye sensitizers and normally also a solid-state

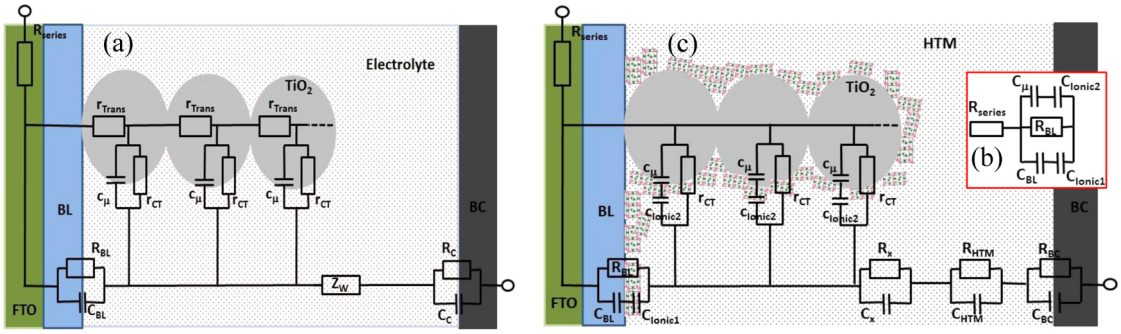

Scheme 1. (a) Equivalent circuit of a liquid DSC with $R_{trans} = L \times r_{trans}$, transport resistance; $R_{CT} = L \times r_{CT}$, charge transfer/recombination resistance; Z_W, Warburg diffusion resistance; R_C/C_C, charge transfer resistance and capacitance at counter electrode; R_{BL}/C_{BL}, charge transfer resistance and capacitance at the FTO or BL, where L is the thickness of the active layer. (b) Full equivalent circuit model of the BL/HTM interface with a mesoporous nonconducting metal oxide at low forward bias. C_{Ionic}, ionic capacitance at the BL interface (1) and at the mesoporous metal oxide interface (2). (c) Full model of a solid-state device with perovskite (R_x/C_x, resistance and capacitance associated with perovskite; R_{HTM}/C_{HTM}, charge transport resistance and capacitance of the HTM; R_{BC}/C_{BC}, charge transfer resistance and capacitance at BC/HTM). Depending on applied bias, the model has to be changed accordingly; see text.

HTM like spiro-MeOTAD. In these devices, the $mTiO_2$ film thickness has been decreased further to the sub-micrometer scale, optimally between 300 and 600 nm. Due to these extremely thin film thicknesses, the pore filling with the HTM is expected to be higher and thus should not be a limiting or irreproducible step. Relative to solid-state or liquid DSCs, this system requires $mTiO_2$ films 10−30 times thinner, respectively. Consequently, the relation between the interface of the compact blocking layer/$mTiO_2$ and the surface area of the latter is considerably altered. Hence, in the case of the system with sub-micrometer mesoporous TiO_2 layers, the influence of the underlayer is much more pronounced. Furthermore, the interplay of the different capacitances (the space charge capacitance of the blocking layer, ionic capacitances in the HTM/blocking layer and HTM/$mTiO_2$ interfaces, and the chemical capacitance of the $mTiO_2$ which is relatively small due to the low active film thickness) will change.

Instead of a layer of dye molecules adsorbed on the surface of the $mTiO_2$, like in the liquid and solid-state DSCs, the perovskite material will cover major areas of the $mTiO_2$ with layers or crystallites having thicknesses of several nanometers. The impact of the degree of $mTiO_2$ coverage by perovskite is unclear and a point of major interest for several reasons. The recombination of electrons from the $mTiO_2$ with holes in the HTM might have to involve an additional step through the perovskite. The conduction band position and/or the charge transport in the $mTiO_2$ can be affected either due to the hindered accessibility for TBP or Li^+ ions, normally crucial for the performance of especially the ssDSCs, or due to the change of the ionic environment by the perovskite coverage.

Impedance spectroscopy (IS) measurements are conducted in order to investigate the internal electrical processes and quantitatively and qualitatively analyze the associated parameters. This study aims to interpret the IS measurements of these devices, using the established equivalent circuits used for DSCs as a starting point and basis for the development of a well-defined model.

In general, IS is nowadays one of the most utilized techniques to analyze liquid DSC devices. Although it is a relatively long procedure from performing the measurement over the fitting of the resulting impedance spectra to the analysis of the extracted data, this technique rewards the investigator with deep insights about the fabricated devices.

For a liquid DSC at intermediate and higher forward biases, a one-channel transmission line model is used (describing the chemical capacitance and the recombination and transport resistance in the TiO_2) in series with an RC element for the counter electrode and, depending on the applied potential, a Warburg diffusion resistance for the ionic transport in the electrolyte (see Scheme 1a). At low forward bias when the mesoporous TiO_2 is insulating, an RC element for the FTO or compact TiO_2 underlayer of the photoanode in contact with the electrolyte has to be employed instead of the transmission line branch for the $mTiO_2$. A modified but similar model is used to simulate the impedance response of ssDSCs.[20,21] In the ssDSC equivalent circuit, an additional RC element has to be implemented instead of the Warburg impedance. The additional RC (R_{HTM} and C_{HTM}) represents the transport of charges inside the HTM if the hole conductor is not doped sufficiently or the hole mobility is too low.

To date, there is only one investigation of perovskite-based solar cells by IS published.[22] It provides valuable information on the capacitive behavior inside these devices, though the behavior of parameters like recombination resistance or transport resistance still remains unclear. Here we present a thorough analysis and provide all the resulting information and subsequent conclusions that can be drawn.

The first comparison in this investigation displays how the DC current and IS response manifests for the

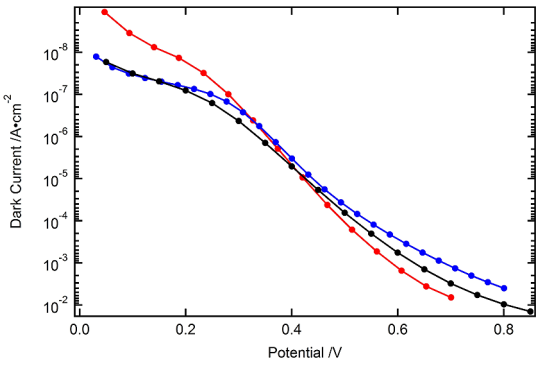

Figure 1. Dark current plotted in log scale against the potential (red, liquid iodine device; blue, solid-state device without perovskite; black, solid-state device with perovskite).

different types of devices utilizing such small active layer thickness. For this reason, the same type of photoanode normally used for the perovskite solar cell was used to build a liquid and a solid-state DSC-type device (without any dye or perovskite adsorbed) using an iodine electrolyte and spiro-MeOTAD, respectively, and comparing it to a standard device with perovskite.

The DC current response of the different device types is presented in Figure 1. In the low forward bias region, the current−voltage characteristic is dominated by the interface photoanode blocking layer (BL)/electrolyte or HTM. It is evident when comparing the current response in this potential region that the dark current in case of the liquid electrolyte is lower, showing the blocking character of this interface toward the triiodide reduction and emphasizing the importance of the blocking layers for the solid-state devices. At higher forward bias from about 400 mV onward, the dark current curve is governed by the current flow over the now conducting $mTiO_2$ (though the magnitude of the currents cannot be compared directly since the Fermi level, E_F, at 0 V differs between the different devices).

In the simplest case, the low forward bias region should be able to be fitted by an RC element for the back contact (BC) or counter electrode and another simple RC accounting for the interface of the compact TiO_2 blocking layer with the hole-transporting agent. The capacitance at the underlayer/hole transport agent interface is, in the liquid DSC, in reality set together out of two capacitances in series, the space charge capacitance in the blocking layer (BL) and the Helmholtz capacitance in the electrolyte. The Helmholtz capacitance is about 10 to 100 times higher and is hence usually disregarded. The simplification of the capacitance at the BL/hole transport (HT) media as in the case of the liquid DSC might not be justified in the case of the solid-state type of devices. In case of the solid-state devices, the capacitance of the underlayer can also be split into two parts. Since we do not have a liquid electrolyte, no "Helmholtz" capacitance can appear. Instead, a capacitance can be formed resulting from the ions (mainly lithium) present in the HTM at this interface. This capacitance is probably on the same order of magnitude as the space charge capacitance of the BL, so it actually cannot be simply discarded similarly to the Helmholtz capacitance in the liquid case. Also, even though the $mTiO_2$ is still insulating in this potential region, and its chemical capacitance, C_μ, is thus still very low, the interplay between C_μ and the capacitance at the interface photoanode blocking underlayer/electrolyte or HTM might play a role. This fact is normally discarded in the equivalent circuit description of a liquid DSC (see Scheme 1a,b) due to its minor influence on the final results. In the case under observation here though, this might play a role and one should keep this in mind in the analysis of the IS measurements. Though Scheme 1b might be the accurate model, it tends to over parametrize the fitting region for this element. The consideration regarding capacitances at the BL/HTM interface can also be applied to the $mTiO_2$/HTM interface. Here too it is questionable if the ionic capacitance in the HTM is high enough to justify discarding it.

Further interesting changes in the fitting procedure include the fact that the transport resistance within such thin layers of $mTiO_2$ will be greatly reduced. The transport resistance increases proportionally with the thickness of the active layer, while the recombination resistance at the same time scales inversely.

The first simplified system to be investigated by IS is the liquid electrolyte-based device with a similar photoanode used for the perovskite devices. In the low forward bias region (not shown here), two semicircles can be identified, the high frequency one relating to the counter electrode and the low frequency one relating to the charge transfer through the BL/electrolyte contact. At higher forward bias, the transport resistance is visible as the 45° straight-line characteristic of the transmission line, as seen in Figure 2a. The transmission line merges toward lower frequencies into the arc representing the recombination resistance and the chemical capacitance of the $mTiO_2$. At even higher forward bias (not shown here), the Warburg diffusion impedance for the diffusion of the ions in the electrolyte appears at low frequencies. Though we have changed the thickness of the $mTiO_2$ by a factor of about 30, the general equivalent circuit model applied for the liquid DSCs has kept its validity.

When considering the Nyquist plot of the solid-state devices (Figure 2b, here for a device with perovskite and spiro-MeOTAD as HTM), we can observe a similar transmission line behavior at intermediate potentials. Consequently, also for the solid-state device, it can be concluded that the transmission line model can be applied as a basic skeleton of an equivalent circuit model. Naturally, the underlying model has to be adjusted according to the bias applied.

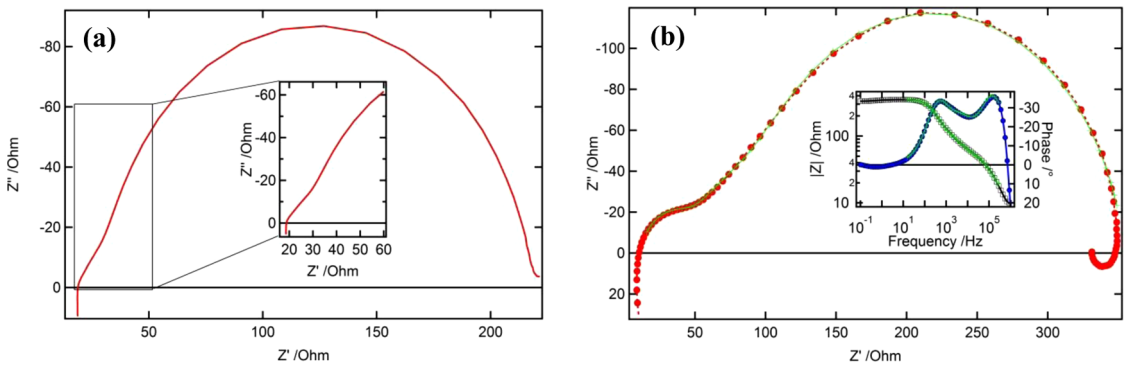

Figure 2. (a) Nyquist plot of the liquid device measured at 560 mV. (b) Nyquist and Bode plot (inset) of a standard solid-state perovskite-based device at 550 mV forward bias. The fit was performed with all parameters nonrestricted except for the exponent of the CPE of the BL. This was fixed to 1 as long as the transmission line was used since no parallel resistance exists for this element and no "real" capacitance can be calculated.

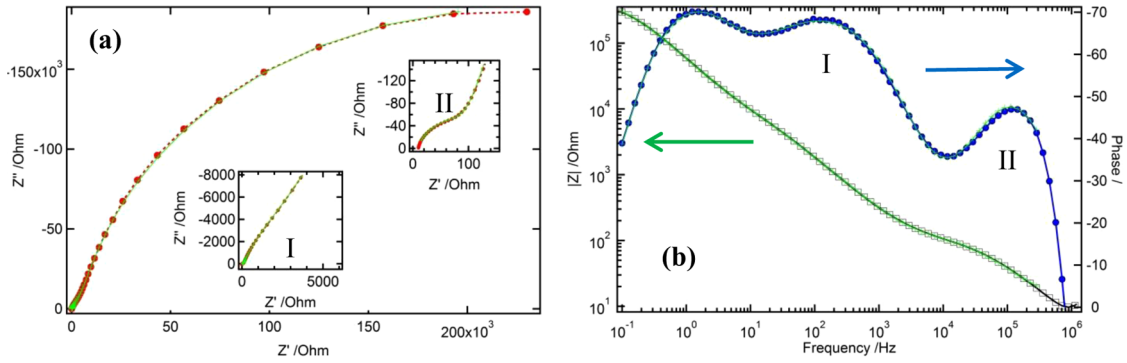

Figure 3. (a) Nyquist and (b) Bode plot of a standard solid-state perovskite-based device at 150 mV forward bias. The green line represents the fit by 3RC elements in series. All elements have been fitted with nonrestricted numbers. The exponent of the CPEs was for all the devices clearly above 0.8. In the case of the mid-frequency RC for the solid-state devices with perovskite, the exponent was 0.78, hence still acceptable. If this value was fixed to 0.8, it did not obviously change the other parameters.

The solid-sate devices show, in the high frequency response, the back contact at the gold/HTM interface, which is similar to the counter electrode interface in the liquid electrolyte device (Figures 2b and 3a,II). This BC element is visible over the whole potential range, staying mainly unchanged in the low forward bias region and beginning to reduce around the maximum power point.

At low forward bias, the samples with the perovskite absorber showed an additional RC element between the low and high frequency semicircles (see Figure 3a,b,I). Such an effect could originate from a poor contact between the compact underlayer and the $mTiO_2$, which would lead to an additional RC element in series to the chemical capacitance in Scheme 1b. Since this element at intermediate frequencies was not visible in the case of the liquid and, more importantly, in case of the solid-state devices without the perovskite, we can exclude a poor contact between the substrate and the $mTiO_2$ and can say that it is directly related to the perovskite. The evolution of the intermediate resistance with potential shows that it is normally constant as long as the current flows over the BL/HTM contact. The resistance decreases steeply with higher forward bias and normally vanishes when dark current starts to flow over the $mTiO_2$.

The deposition technique of the perovskite from a solution mixture of PbI_2 and CH_3NH_3I precursors in GBL used here shows the formation of distributed crystallites of the absorber on the TiO_2. As such, the control over the perovskite crystallization, stoichiometry, and morphology is poor. However, contrary to Ball *et al.*,[5] no conformal film on top of the $mTiO_2$ film is present, though coverage is believed to be high with high fraction of pore filling. As a result, charge transport can flow *via* the "known" mechanism from ssDSC or *via* the perovskite itself or *via* a combination of both pathways. However, when using this material, the hole transport is believed to be directed mainly by the hole conductor, spiro-MeOTAD, which is not the case when $PbCl_2$ is used[4,5] in place of PbI_2.

When taking a closer look at the potential region with forward biases near V_{OC}, the $mTiO_2$ is in its conductive state, and the transmission line has vanished, we would expect a two RC response of the different devices. One represents the BC interface (at high frequencies) and the other (at low frequencies) the $mTiO_2$/HTM interface.

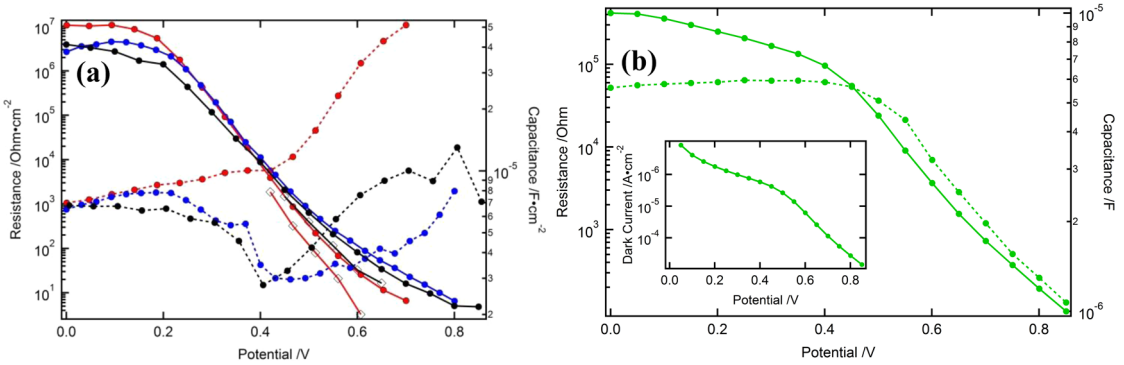

Figure 4. (a) Transport R_{trans} (open squares) and recombination resistance R_{ct} (solid circles) as well as the chemical capacitance (dashed circles) of a liquid device (red) and solid-state devices with (black) and without (blue) perovskite with a similar photoanode. (b) Recombination resistance and associated capacitance of a perovskite solid-state device with mesoporous Al_2O_3 instead of mesoporous TiO_2. Inset shows the dark current during the measurement.

In the low frequency region at high forward bias, the solid-state devices show a slow time constant phenomenon. It can appear as a so-called "negative capacitance" or, and maybe with a similar origin as the negative capacitance, as an additional small semicircle at frequencies in the low hertz or millihertz range (see Figure 2b). Interestingly, this feature can have an increasing (additional RC element) or a decreasing (negative capacitance) effect on the overall DC resistance. The origin of such a negative capacitance is normally assumed to be based on an imbalance (or a nonohmic behavior) at one of the extracting contacts.[23,24] It leads sometimes to a cross over or roll over effects in the $J-V$ curves.[25] This effect appears in most of the cases at high electron density in the semiconductor. Since it is clearly related to slow time constants, it might be related to the reorganization of mobile ions at one of the interfaces.

In the case of the devices with perovskite, at higher applied potential, an additional intermediate semicircle is sometimes visible in the mid-frequency region, so between the BC and the recombination RC features (similar to the case of low forward bias). Since there is no clear indication if and how these two elements in the mid-frequency range are related, they were treated simply as an additional RC element in series with the others (R_x and C_x in Scheme 1c). After observation on how these two elements behave, we can rethink what could be their origin and modify the model accordingly.

To further study the samples and their IS response, we applied the proposed models for the fitting procedure though omitting the ionic capacitances and the element related to the HTM if not stated otherwise.

Returning to the three model systems (liquid device without perovskite and solid-state devices with and without perovskite), it was found that the behavior of all three samples is indeed quite similar as already implied by the current characteristics. The main feature to change is the behavior of the chemical capacitance (see Figure 4a). Initially, at low forward bias, the determined low frequency resistance (the charge transfer at the BL/HT media interface) resembles clearly the tendencies of the dark current. The capacitance in this potential region is dominated by the capacitance at the BL/HT media interface, and the determined values are all on the same order of magnitude. The capacitance in the case of the liquid device increases slightly with increasing forward bias as long as the dark current is channeled over the BL. In the case of the solid-state devices, the capacitance first increases before it suddenly drops. The drop in capacitance near 400 mV forward bias for the two types of solid-state devices was also observed for dye-sensitized solid-state devices and can be explained by a drop of the capacitance at the BL/HTM interface.[20] For comparison, the low frequency arc capacitance for a device with mAl_2O_3 instead of mTiO_2 (see Figure 4b) was also determined. In this case, the capacitance dropped with increasing potential, showing the plane evolution of the capacitance at this interface with increasing potential without the overlaid increase of the chemical capacitance of the mTiO_2.

The chemical capacitance in the mTiO_2 increases (at an applied forward bias >400 mV), and the transport resistance becomes visible. The chemical capacitances of the three devices display different behavior relative to the increase in potential. The increase of the capacitance is most pronounced in the liquid device type. The increase in the solid-state device with perovskite is steeper compared to the solid-state device without perovskite. Clearly, the ionic environment of the mTiO_2 is different in each device. This can lead to changes in the shape of the density of trap states (DOS) inside the mTiO_2 and therefore of the chemical capacitance. In this aspect, the difference in the C_μ between the two solid-state devices is particularly interesting. The perovskite obviously has an influence on the shape and population of the DOS.

The electron lifetime, τ_n, can be determined from the recombination resistance and the chemical capacitance using $\tau_n = R_{ct} \times C_\mu$. This chemical capacitance,

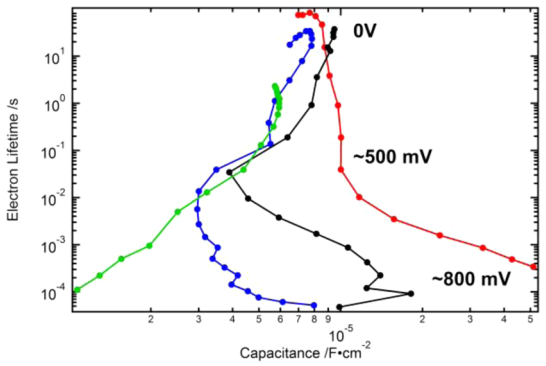

Figure 5. Electron lifetime as a function of the capacitance (red, liquid iodine electrolyte-based device; black, solid-state device with perovskite; blue, solid-state device without perovskite; green, solid-state device with perovskite using mAl_2O_3).

C_μ, is directly proportional to the DOS dependent on the dimension specifications of the mesoporous TiO_2 film. Electron lifetimes for the different types of devices are presented in Figure 5. The lifetimes are plotted against chemical capacitance of the $mTiO_2$ since the direct comparison of the lifetimes against the applied voltage is not suitable under such conditions. The conduction band position and the redox potential of the HT media differ for the different systems under consideration. Normally, under the assumption of a similar distribution of bulk traps inside the TiO_2, one can use the chemical capacitance of the $mTiO_2$ or the DOS as an indirect measure of the Fermi level or more precisely as a measure of the distance of the Fermi level (E_F) to the conduction band. However, the systems investigated in Figures 4 and 5 do not meet this criterion. The perovskite and additives like lithium ions or TBP change the conduction band position and change the ionic surroundings of the $mTiO_2$ and can therefore also change the distribution of the density of states, as shown in Figure 4a. It would also be possible to use the conductivity of the $mTiO_2$ to compare different samples since it represents under certain conditions the same number of mobile charge carriers in the conduction band (E_{cb}). However, the transport of charges is also greatly influenced by the ionic surrounding (screening) of the $mTiO_2$, and the transport resistance necessary to calculate the conductivity can only be determined in a small potential range, which results in a small window to compare the properties of the investigated samples. The chemical capacitance is therefore the best possibility to get at least an idea about the relation of electron lifetime and E_F, although one should keep the mentioned restrictions in mind.

In the low forward bias region, all four samples (including the mAl_2O_3 sample) possess very similar electron lifetimes since the current flows over the BL, which should be more or less similar for all devices. When looking in the region in which the $mTiO_2$ is active, the lifetime is the longest for the devices with the liquid electrolyte in combination with the iodine redox system. It is followed by the lifetime in solid-state devices with perovskite and finally the lowest lifetime for the solid-state device with only the spiro-MeOTAD/TiO_2 interface (without perovskite). The data presented in green are the electron lifetime with a device with mAl_2O_3 instead of the $mTiO_2$ where all the dark current can only be driven over the compact TiO_2 BL/HTM interface.

The mAl_2O_3 sample clearly shows no increase of the capacitance with higher forward bias (see Figure 4b). On the contrary, the capacitance drops at higher potential. Such a behavior was already observed for ssDSC-type devices using ZrO_2 in place of $mTiO_2$ but utilizing thicker mesoporous films.[20,23,24]

We can conclude on the basis of these results that charge (electron) transport is channeled over the mesoporous oxide as evidenced by the observation of the chemical capacitance of the mesoporous TiO_2. This capacitance belongs to the low frequency arc in the Nyquist plot and that this RC element relates to the $mTiO_2$ is further indicated by the fact that its resistance scales with the TiO_2 thickness as shown already in the publication of Kim *et al.*[3] Another result which supports our conclusion is presented in the publication by Abrusci *et al.*[26] in which the capacitance determined by charge extraction measurements is much smaller for the case in which the electrons are not injected into a $mTiO_2$ but a fullerene layer.

One can also observe that the BL can dominate the observed lifetimes to different extents (Figure 5). The easier the recombination over the BL at lower potential, the more current is driven over this interface and the more forward bias has to be applied to "activate" the mesoporous oxide (see the case of the solid-state device without perovskite where the increase in chemical capacitance is at a higher forward bias compared to the sample with perovskite).

The investigation of these model systems allowed the identification and analysis of the individual components contributing to the IS response. We have developed a procedure and appropriate models that can be used to fit the data generated with perovskite samples; see section I of the Supporting Information for a full description of this fitting procedure.

Influence of Spiro-MeOTAD Overlayer Thickness and HTM Additive Concentrations. By changing the deposition conditions of the perovskite solution (spinning speed and HTM solution concentration), the thickness of the spiro-MeOTAD overlayer on top of the $mTiO_2$ was varied and the resultant devices were characterized by $J-V$ measurements and IS. The suggested equivalent circuit model was used to fit the data, verifying the physical meaning of the individual IS parameters. This analysis was then used to correlate and explain the changes in the device performance as a function of the overlayer thickness (see section II of Supporting Information). It was found that, for a HTM overlayer

thickness between 0 and 136 nm, the HTM forms a conformal overlayer, blocking the direct contact between the perovskite and the gold back contact, thus leading to an increase in the V_{OC} and the J_{SC} of solar cells. In our previous work,[20] the charge transport resistance of the spiro-MeOTAD was shown to manifest as an RC arc at high to intermediate frequencies in the Nyquist plots. For thin HTM overlayers up to 140 nm, the magnitude of the high frequency resistance is similar and hence attributed to the charge transport resistance at the back contact (BC)/HTM interface, as the transport resistance of the HTM is too small to be resolved for such thin overlayers. As the HTM overlayer is increased above 136 nm, the increase in series resistance arising from the increasingly large charge transport resistance values of the spiro-MeOTAD (Figure 6) leads to a decrease in the fill factor (FF) and thus in the overall cell power conversion efficiency (PCE), reflected in the drop in J_{SC} and V_{OC}.

Furthermore, the influence of the common additives to the HTM solution, LiTFSI and TBP, on the IS parameters was investigated (see sections III and IV of Supporting Information). These displayed similar effects as already known from the study of ssDSCs and liquid DSCs, confirming the validity of the IS equivalent circuit applied to the analysis here. In the case of LiTFSI, the role of lithium ions is rather complex, where the presence of Li^+ is known to influence the doping mechanism of the spiro-MeOTAD[27,28] as well as the mobility of charges. Devices without any LiTFSI content displayed an additional resistive element (see Supporting Information Figure S12) that is most likely related to the transport resistance in the HTM. Li^+ also plays a role in the screening of the negative charge of the electrons inside the $mTiO_2$ enabling a facilitated charge transport,[29] and the lithium ions were observed to induce a shift of the conduction band of the $mTiO_2$ to lower voltage. The increasing content of the Li^+ ions moreover was found to influence the shape of the DOS and increase the lifetime of the electrons.

In the case of TBP, it was found that it acts as a recombination blocking agent, hence increasing the recombination resistance for the electrons at high TBP content. Additionally, as in the case of conventional DSCs,[30−34] the TBP leads to an upward shift in the conduction band edge of the $mTiO_2$, which is observed in the chemical capacitance (see Supporting Information Figure S18). This directly influences the V_{OC} of the devices, leading to an increase in V_{OC} as the conduction band is shifted upward with increasing TBP concentration. The increase in concentration of TBP also results in an increase of the series resistance, leading to lower FF of devices. Pyridine compounds such as TBP are known to adsorb onto gold electrodes[35] and therefore act as a blocking layer for the charge transfer at the interface between the gold and the HTM. Furthermore, the high binding strength of TBP results in a decreased concentration of "free" Li ions, leading additionally to an increasing of the series resistance as the transport resistance of the HTM becomes larger as the spiro-MeOTAD is less p-doped.

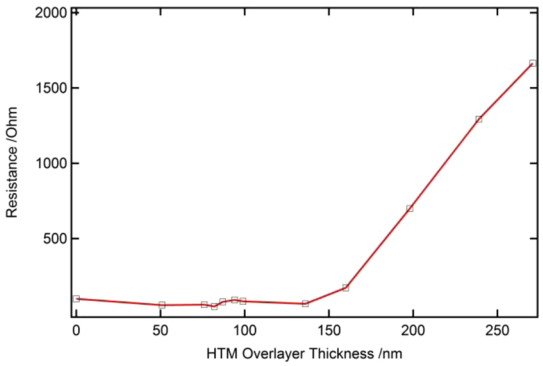

Figure 6. Magnitude of the high frequency resistance determined at a corrected potential of 0.2 V as a function of the HTM overlayer thickness.

TABLE 1. PCE Values for a Device Scanned with Different Velocities[a]

scan velocity (mV s^{-1})	J_{SC} (mA cm^{-2})	V_{OC} (V)	FF	efficiency (%)
200 B	16.07	0.85	0.72	9.69
200 F	16.07	0.83	0.54	7.19
100 B	15.74	0.84	0.72	9.50
100 F	15.67	0.84	0.58	7.62
50 B	15.35	0.84	0.72	9.30
50 F	15.30	0.84	0.62	7.90
10 B	14.80	0.84	0.72	8.94
10 F	14.78	0.84	0.67	8.33

[a] Here from V_{OC} to 0 V and back, F = 0 V to V_{OC} (forward scan), B = V_{OC} to 0 V (backward scan).

Standard Devices under Illumination. So far, the devices were only investigated under dark conditions. The impedance measurements revealed that most of the basic concepts from related devices like DSCs and ssDSCs keep their validity. However, differences also appear such as the additional semicircle at intermediate frequencies and, for example, the behavior of J_{SC} and V_{OC} with increasing HTM overlayer.

There exists a strong hysteresis in the $J-V$ curves under illumination (see section V in Supporting Information Figure S20), which manifests mainly only in the forward scan (from low to high forward bias). Such an effect is not detectable in the dark measurements. The PCE values for the different scan velocities can be seen in Table 1. The backward scan from high to low forward bias showed nearly no dependence on scan velocity. On the other hand, the efficiency of the forward scan from low to high forward bias is strongly velocity-dependent, indicating that some slow charged carriers are involved in the current and voltage generation.

In the transient photocurrent dynamics, slow reaction times of the perovskite devices can similarly be observed (Supporting Information Figure S21).

The current dynamics show first a steep rise of the current after the red light LED pulse, which decays fast. After this initial fast decay, a slow rise of the photocurrent can be observed. After the red light pulse is stopped, a fast decay of the photocurrent is followed by a slow decay. A similar observation can be seen for the photovoltage rise and decay after the light pulse. The fitting procedure included two exponentials, one used to fit the fast rise and decay and the other exponential for the slow component. The time constant for the slow component of the photocurrent yields a time constant of about 16 ms for the rise and 15 ms for the decay. The time constant associated with the photovoltage rise and decay is 32 and 26 ms, respectively.

Such an effect should manifest in the IS measurements, and indeed, a slow time constant phenomena can be observed under illumination (Figure 7).

This poses the question of the origin of this slow process, which clearly has an influence on the PCE of such devices. There are several possibilities for such an effect, mainly ionic charge transport, ion intercalation, or it might even be a ferroelectric effect. Generally, it is clear that this feature is mainly a light-induced effect, as it does not appear to the same extent for measurements conducted under dark conditions. To further examine this process, a perovskite device without HTM was built and measured under illumination to verify if such a slow phenomenon is still observable. Indeed, such a phenomena can be detected in the IS response. Hence, this excludes a photointercalation phenomenon as a possible origin. As described above, we could observe an additional resistive element under dark conditions at low forward bias attributed to a charge transport through the perovskite. This feature was observed to vanish under illumination. This shows that the ability of this perovskite interfacial layer to transport charges is strongly increased under illumination. The electronic conductivity of the perovskite layer will be high under illumination, but some charge carriers seem to be transported by ions. Furthermore, we cannot fully exclude other possible contributions like the previously mentioned ferroelectric effect.[36]

Apart from the slow component in the Nyquist plot, two different elements can be observed under illumination: the high frequency RC for the BC/HTM interface and the element associated with the chemical capacitance and the recombination resistance of the $mTiO_2$. At lower light intensities, a third element, a transmission line for the transport inside the TiO_2, is also visible.

The $J-V$ characteristic and a comparison of the IS fitting results in the dark and under illumination can be seen in Figure 8a,b, respectively. One can clearly observe the similar behavior of the increasing chemical capacitance at high forward bias in the dark and under illumination, while the recombination resistance as well as the transport resistance for the electrons is

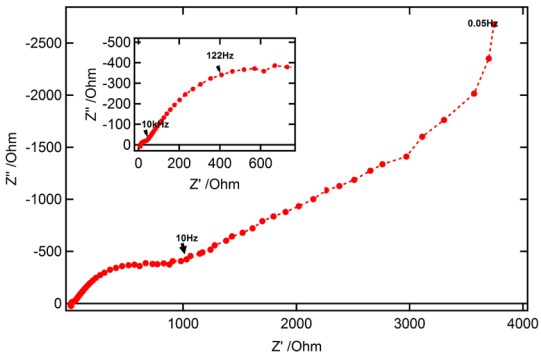

Figure 7. Nyquist plot of a standard device under illumination at 0 V. Inset shows the frequencies from the MHz down to about 10 Hz.

greatly reduced when under illumination. The charge collection efficiency, η_{cc}, which can be calculated according to $\eta_{cc} = 1/(1 + (\tau_{trans}/\tau_n))$, shows about 80−85% (see Supporting Information Figure S22). As already observed in the relationship between the transport and recombination resistance in the dark (see Figure 8b), the charge collection efficiency is one of the critical parameters for reaching high photocurrent in such devices. As visible at 40% light intensity, the charge collection efficiency is considerably lower than in the case of a typical liquid DSC, which is generally over 95% also at full sunlight intensity. Increasing to 100% light intensity for such perovskite devices leads to further reduction in η_{cc} to below 80%. This shows that by the applied fitting procedure one identifies a key parameter which has to be further optimized in such devices, the charge collection efficiency. As clearly found in this investigation, the J_{SC} can still be improved in this type of devices when, for example, reducing the recombination while maintaining a similar transport resistance. This would lead to an increased J_{SC} and V_{OC} and finally to an overall increased device efficiency.

Final Statements. As mentioned above, the IS response associated with the perovskite at intermediate frequencies needs to be addressed. We believe that there is injection of charge carriers from and to the perovskite with the TiO_2. This could be clearly shown by the change of the capacitance associated with the recombination arc generating the current (Figure 4) and in the publications of Abrusci *et al.*[26] Without $mTiO_2$, no real increase in the capacitance is visible (with the simplification mentioned for the fitting procedure from Scheme 1b to 1c), showing that the capacitance can be used as a clear indicator for the active part of the $mTiO_2$ in the charge transfer processes. The origin of the RC element at intermediate frequencies at low forward bias in the dark is, as already mentioned above, most probably related to the perovskite. This element is quite insensitive to any of the treatments presented here except for the case of the low TBP content. This is explained by the indirect effect

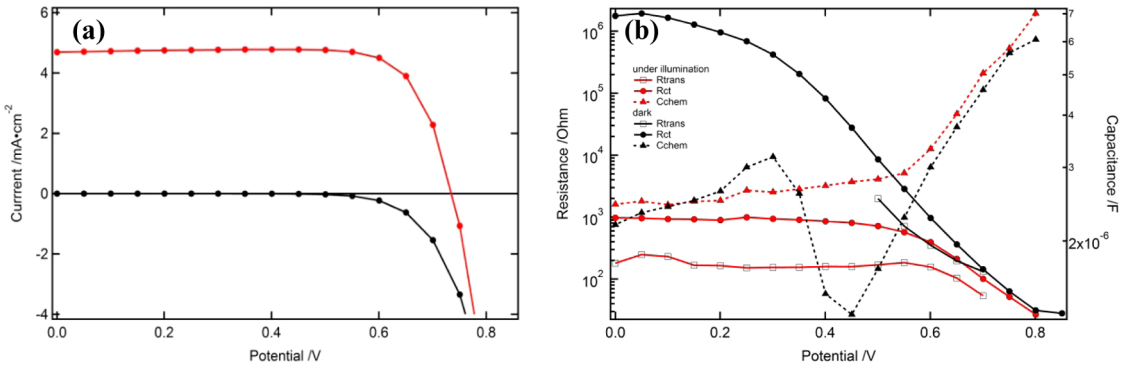

Figure 8. (a) Current−voltage characteristic in the dark (black) and under illumination at 40% sun light intensity by LED (red). (b) Extracted impedance result of the recombination resistance (solid circles), the transport resistance (open squares), and the chemical capacitance (dashed triangles).

of the TBP binding with the Li^+ ions decreasing the concentration of "free" Li^+ ions, thus leading to an increase in the transport resistance of the perovskite and the HTM. As we believe that there is a relatively conformal film of the perovskite on top of the BL and on the $mTiO_2$, charges have to be channeled *via* this perovskite film. As such, it acts like an intermediate layer between the $mTiO_2$ and the HTM. This is further validated by the disappearance of this feature when the devices are under illumination and the perovskite is very conductive.

CONCLUSIONS

In this work, solid-state mesoscopic solar cells using lead-iodide-based perovskite deposited onto sub-micrometer thick mesoporous TiO_2 in combination with spiro-MeOTAD as a HTM are investigated using IS. Through comparison with the well-known liquid and solid-state DSC systems, these devices are analyzed and interpreted, systematically establishing an equivalent circuit model that can be applied to the IS analysis of this type of devices. This model is then employed to explore the effect of the concentration variation of the common HTM solution additives, TBP and LiTFSI, on the device parameter. Additionally, the influence of the overlayer thickness of the HTM on top of the $mTiO_2$ is investigated. From these experiments, the working mechanism of these perovskite devices is explored and the presented model used for the IS interpretation is validated. The complex nature of this system is exposed, and the interplay of various components (*i.e.*, additive ratios) is highlighted. The experimental results show the multiple roles and effects of the Li^+ ion and TBP concentrations in the HTM on the internal electrical parameters and consequently on the overall device performance.

The model presented further identifies the separate features corresponding to the electronic and presumably ionic conductivities of the lead-iodide-based perovskite material. These features are unique to this system and are believed to greatly depend on the morphology and nature of the perovskite material as these define its transport and electrical properties. As such, this investigation shows that IS is a useful tool for characterizing this type of system, and the developed IS model can be applied to examine the perovskite material in working device configurations to identify the limiting processes reducing the overall efficiency of the solar cells.

METHODS

Materials. All chemicals were purchased from Sigma-Aldrich and used as received. 2,2′,7,7′-Tetrakis(*N*,*N*-di-*p*-methoxyphenylamine)-9,9′-spirobifluorene (spiro-MeOTAD) was purchased from Merck and used as received. The CH_3NH_3I precursor was synthesized in our laboratory.

Device Fabrication. Fluorine-doped tin oxide (FTO)-coated glass substrates (TEC 15, Pilkington) were patterned by laser etching to give the desired electrode configuration. After undergoing thorough cleaning by mechanical scrubbing using Hellmanex, ultrasonication, and finally ozone cleaning, a TiO_2 compact layer was deposited on the substrates by spray pyrolysis at 450 °C using the precursor titanium diisopropoxide bis(acetylacetonate) diluted in ethanol (1:10 volume ratio) and oxygen as the carrier gas. The substrates were subsequently immersed in a 0.02 M aqueous solution of $TiCl_4$ for 30 min at 70 °C, after which they were rinsed with water and heated at 500 °C for 20 min. The sub-micrometer mesoporous TiO_2 layer was deposited by spin-coating TiO_2 paste (Dyesol 18NR-T) diluted in ethanol at 1:2.5 by weight at 2000 rpm. The films were heated stepwise to 500 °C at which they were sintered for 15 min. While still hot, the substrates were transferred into a drybox. All subsequent deposition steps were carried out under dry conditions. The perovskite precursor solution was prepared as reported by Kim *et al.*[3] A 1:1 molar ratio mixture of PbI_2 and CH_3NH_3I was dissolved in γ-butyrolactone (GBL) at 30 wt % by heating at 60 °C overnight. This solution was deposited onto the $mTiO_2$ films by spin-coating at 2000 rpm for 30 s. The films were then annealed at 100 °C for 5−10 min and cooled to room temperature. The color of the films was observed to change from yellow to dark brown. The standard hole transport material solution was prepared by dissolving 0.059 M spiro-MeOTAD in chlorobenzene, to which 1% molar ratio of cobalt(III) dopant, 0.05 M *tert*-butylpyridine (TBP), and 0.009 M $Li[(CF_3SO_2)_2N]$ (LiTFSI) were added. Both the cobalt(III) complex, tris(2-(1*H*-pyrazol-1-yl)-4-*tert*-butylpyridine)cobalt(III)-tris(bis(trifluoromethylsulfonyl)imide)), coded FK209, and the LiTFSI salt were

predissolved in acetonitrile. The HTM solution was deposited on the perovskite-sensitized films by spin-coating at 4000 rpm for 30 s unless specified otherwise. The devices were completed by thermal evaporation of 60 nm of Au counter electrode. Cells were not sealed but stored in the dark under dry conditions. The counter electrode of the liquid DSC was a thermally deposited Pt. The counter electrode was attached to the substrate with the $mTiO_2$ by a hot melt polymer. The electrolyte injected before sealing the device is coded Z952.

Impedance Measurements. The impedance measurements were performed using a Bio-Logic SP300 potentiostat. A dc potential bias was applied and overlaid by a sinusoidal ac potential perturbation of 15 mV over a frequency range of 7 MHz to 0.1 Hz (for the measurements under illumination, the lowest frequency is 0.01 Hz). The applied dc potential bias was changed by ~50 mV steps from 850 to 0 mV. The resulting impedance spectra were fitted using the ZView software (Scribner Associates Inc.).

Transient Measurements. The transient photovoltage and photocurrent measurement setup is similar to the description by O'Regan *et al.*[37,38] White bias light was provided by an array of diodes (Lumiled model LXHL-NWE8 white star). For the small perturbation, red-light-pulsed diodes (LXHLND98 redstar, 0.2 s square pulse width, 100 ns rise and fall time) were used, controlled by a fast solid-state switch. The voltage dynamics were recorded *via* a Keithley 2602 sourcemeter. The voltage decay measurements were performed from zero current (V_{OC}). Small perturbation transient photocurrent measurements were performed in a similar way to the open-circuit voltage decay measurements but here holding a fixed potential while measuring the photocurrent transients. The decays were fitted with a double exponential decay.

Conflict of Interest: The authors declare no competing financial interest.

Acknowledgment. We acknowledge financial support from Aisin Cosmos R&D Co., Ltd., Japan, and from the European Community's Seventh Framework Programme (FP7/2007-2013) under the "ORION" Grant Agreement No. NMP-229036. M.G. thanks the European Research Council for an Advanced Research Grant ARG 247404 funded under the "Mesolight" project. M.K.N. thanks the World Class University programs (Photovoltaic Materials, Department of Material Chemistry, Korea University), funded by the Ministry of Education, Science and Technology through the National Research Foundation of Korea (R31-2008-000-10035-0).

Supporting Information Available: IS fitting procedure, transient current and photovoltage dynamics, $J-V$ characteristic at a scan velocity of 100 mV/s, recombination resistance, capacitance and dark current measurement of perovskite solid-state device using mesoporous Al_2O_3 in place of $mTiO_2$, charge collection efficiency of standard perovskite solid-state device under 40% sun intensity, experimental data and additional discussion on variation of TBP and LiTFSI additive concentrations and HTM overlayer thickness. This material is available free of charge *via* the Internet at http://pubs.acs.org.

REFERENCES AND NOTES

1. Im, J.-H.; Lee, C.-R.; Lee, J.-W.; Park, S.-W.; Park, N.-G. 6.5% Efficient Perovskite Quantum-Dot-Sensitized Solar Cell. *Nanoscale* **2011**, *3*, 4088–4093.
2. Chung, I.; Lee, B.; He, J.; Chang, R. P. H.; Kanatzidis, M. G. All-Solid-State Dye-Sensitized Solar Cells with High Efficiency. *Nature* **2012**, *485*, 486–489.
3. Kim, H.-S.; Lee, C.-R.; Im, J.-H.; Lee, K.-B.; Moehl, T.; Marchioro, A.; Moon, S.-J.; Humphry-Baker, R.; Yum, J.-H.; Moser, J.-E.; *et al.* Lead Iodide Perovskite Sensitized All-Solid-State Submicron Thin Film Mesoscopic Solar Cell with Efficiency Exceeding 9%. *Sci. Rep.* **2012**, *2*, 591.
4. Lee, M. M.; Teuscher, J.; Miyasaka, T.; Murakami, T. N.; Snaith, H. Efficient Hybrid Solar Cells Based on Meso-Superstructured Organometal Halide Perovskites. *Science* **2012**, *338*, 643–647.
5. Ball, J. M.; Lee, M. M.; Hey, A.; Snaith, H. Low-Temperature Processed Meso-Superstructured to Thin-Film Perovskite Solar Cells. *Energy Environ. Sci.* **2013**, *6*, 1739–1743.
6. Etgar, L.; Gao, P.; Xue, Z.; Peng, Q.; Chandiran, A. K.; Liu, B.; Nazeeruddin, M. K.; Grätzel, M. Mesoscopic $CH_3NH_3PbI_3/TiO_2$ Heterojunction Solar Cells. *J. Am. Chem. Soc.* **2013**, *134*, 17396–17399.
7. Misusaki, J.; Arai, K.; Fueki, K. Ionic Conduction of the Perovskite-Type Halides. *Solid State Ionics* **1983**, *11*, 203–211.
8. Inaguma, Y.; Liquan, C.; Itoh, M.; Nakamura, T.; Uchida, T.; Ikuta, H.; Wakihara, M. High Ionic Conductivity in Lithium Lanthanum Titanate. *Solid State Commun.* **1993**, *86*, 689–693.
9. Mitzi, D. B. Solution-Processed Inorganic Semiconductors. *J. Mater. Chem.* **2004**, *14*, 2355–2365.
10. Kagan, C.; Mitzi, D.; Dimitrakopoulos, C. Organic–Inorganic Hybrid Materials as Semiconducting Channels in Thin-Film Field-Effect Transistors. *Science* **1999**, *286*, 945–947.
11. Billing, D. G.; Lemmerer, A. Inorganic–Organic Hybrid Materials Incorporating Primary Cyclic Ammonium Cations: The Lead Iodide Series. *CrystEngComm* **2007**, *9*, 236–244.
12. Mitzi, D. B.; Chondroudis, K.; Kagan, C. R. Design, Structure, and Optical Properties of Organic-Inorganic Perovskites Containing an Oligothiophene Chromophore. *Inorg. Chem.* **1999**, *38*, 6246–6256.
13. Fluegel, B.; Zhang, Y.; Mascarenhas, A.; Huang, X.; Li, J. Electronic Properties of Hybrid Organic–Inorganic Semiconductors. *Phys. Rev. B* **2004**, *70*, 205308.
14. Mitzi, D. B.; Feild, C. A.; Harrison, W. T. A.; Guloy, A. M. Conducting Tin Halides with a Layered Organic-Based Perovskite Structure. *Nature* **1994**, *369*, 467–469.
15. Chang, Y. H.; Park, C. H.; Matsuishi, K. First-Principles Study of the Structural and the Electronic Properties of the Lead-Halide-Based Inorganic–Organic Perovskites $(CH_3NH_3)PbX_3$ And $CsPbX_3$ (X = Cl, Br, I). *J. Korean Phys. Soc.* **2004**, *44*, 889–893.
16. Noh, J. H.; Im, S. H.; Heo, J. H.; Mandal, T. N.; Seok, S. I. Chemical Management for Colorful, Efficient, and Stable Inorganic–Organic Hybrid Nanostructured Solar Cells. *Nano Lett.* **2013**, *13*, 1764–1769.
17. Bi, D.; Yang, L.; Boschloo, G.; Hagfeldt, A.; Johansson, E. M. J. Effect of Different Hole Transport Materials on Recombination in $CH_3NH_3PbI_3$ Perovskite-Sensitized Mesoscopic Solar Cells. *J. Phys. Chem. Lett.* **2013**, *4*, 1532–1536.
18. Heo, J. H.; Im, S. H.; Noh, J. H.; Mandal, T. N.; Lim, C.-S.; Chang, J. A.; Lee, Y. H.; Kim, H.-J.; Sarkar, A.; Nazeeruddin, M. K.; *et al.* Efficient Inorganic–Organic Hybrid Heterojunction Solar Cells Containing Perovskite Compound and Polymeric Hole Conductors. *Nat. Photonics* **2013**, *7*, 486–491.
19. Edri, E.; Kirmayer, S.; Cahen, D.; Hodes, G. High Open-Circuit Voltage Solar Cells Based on Organic–Inorganic Lead Bromide Perovskite. *J. Phys. Chem. Lett.* **2013**, *4*, 897–902.
20. Dualeh, A.; Moehl, T.; Nazeeruddin, M. K.; Grätzel, M. Temperature Dependence of Transport Properties of Spiro-MeOTAD as a Hole Transport Material in Solid-State Dye-Sensitized Solar Cells. *ACS Nano* **2013**, *7*, 2292–2301.
21. Boix, P. P.; Larramona, G.; Jacob, A.; Delatouche, B.; Mora-Sero, I.; Bisquert, J. Hole Transport and Recombination in All-Solid Sb_2S_3-Sensitized TiO_2 Solar Cells Using CuSCN as Hole Transporter. *J. Phys. Chem. C* **2012**, *116*, 1579–1587.
22. Kim, H.-S.; Mora-Sero, I.; Gonzalez-Pedro, V.; Fabregat-Santiago, F.; Juarez-Perez, E. J.; Park, N.-G.; Bisquert, J. Mechanism of Carrier Accumulation in Perovskite Thin-Absorber Solar Cells. *Nat. Commun.* **2013**, *4*, 2242.
23. Bisquert, J. A Variable Series Resistance Mechanism To Explain the Negative Capacitance Observed in Impedance Spectroscopy Measurements of Nanostructured Solar Cells. *Phys. Chem. Chem. Phys.* **2011**, *13*, 4679–4685.
24. Mora-Sero, I.; Bisquert, J.; Fabregat-Santiago, F.; Garcia-Belmonte, G.; Zoppi, G.; Durose, K.; Proskuryakov, Y.; Oja, I.; Belaidi, A.; Dittrich, T.; *et al.* Implications of the Negative Capacitance Observed at Forward Bias in Nanocomposite

and Polycrystalline Solar Cells. *Nano Lett.* **2006**, *6*, 640–650.
25. Eisenbarth, T.; Caballero, R.; Nichterwitz, M.; Kaufmann, C. A.; Schock, H.-W.; Unold, T. Characterization of Metastabilities in Cu(In,Ga)Se_2 Thin-Film Solar Cells by Capacitance and Current–Voltage Spectroscopy. *J. Appl. Phys.* **2011**, *110*, 094506-13.
26. Abrusci, A.; Stranks, S. D.; Docampo, P.; Yip, H.-L.; Jen, A.-K. Y.; Snaith, H. High-Performance Perovskite-Polymer Hybrid Solar Cells *via* Electronic Coupling with Fullerene Monolayers. *Nano Lett.* **2013**, *13*, 3124–3128.
27. Abate, A.; Leijtens, T.; Pathak, S.; Teuscher, J.; Avolio, R.; Errico, M. E.; Kirkpatrik, J.; Ball, J. M.; Docampo, P.; McPherson, I.; *et al.* Lithium Salts as "Redox Active" p-Type Dopants for Organic Semiconductors and Their Impact in Solid-State Dye-Sensitized Solar Cells. *Phys. Chem. Chem. Phys.* **2013**, *15*, 2572–2579.
28. Snaith, H.; Grätzel, M. Enhanced Charge Mobility in a Molecular Hole Transporter *via* Addition of Redox Inactive Ionic Dopant: Implication to Dye-Sensitized Solar Cells. *Appl. Phys. Lett.* **2006**, *89*, 262114-3.
29. Kambe, S.; Nakade, S.; Kitamura, T.; Wada, Y.; Yanagida, S. Influence of the Electrolytes on Electron Transport in Mesoporous TiO_2–Electrolyte Systems. *J. Phys. Chem. B* **2002**, *106*, 2967–2972.
30. Koops, S. E.; O'Regan, B.; Barnes, P. R. F.; Durrant, J. R. Parameters Influencing the Efficiency of Electron Injection in Dye-Sensitized Solar Cells. *J. Am. Chem. Soc.* **2009**, *131*, 4808–4818.
31. Katoh, R.; Kasuya, M.; Kodate, S.; Furube, A.; Fuke, N.; Koide, N. Effects of 4-*tert*-Butylpyridine and Li Ions on Photoinduced Electron Injection Efficiency in Black-Dye-Sensitized Nanocrystalline TiO_2 Films. *J. Phys. Chem. C* **2011**, *113*, 20738–20744.
32. Howie, W. H.; Harris, J. E.; Jennings, J. R.; Peter, L. M. Solid-State Dye-Sensitized Solar Cells Based on Spiro-MeOTAD. *Sol. Energy Mater. Sol. Cells* **2007**, *91*, 424–426.
33. Dürr, M.; Rosselli, S.; Yasuda, A.; Nelles, G. Band-Gap Engineering of Metal Oxides for Dye-Sensitized Solar Cells. *J. Phys. Chem. B* **2006**, *110*, 21899–21902.
34. Zhao, Y.; Chen, W.; Zhai, J.; Sheng, X.; He, Q.; Wei, T.; Bai, F.; Jiang, L.; Zhu, D. Solid-State Dye-Sensitized Photovoltaic Device with Newly Designed Small Organic Molecule as Hole-Conductor. *Chem. Phys. Lett.* **2007**, *445*, 259–264.
35. Jurkiewicz-Herbich, M.; Slojkowska, R.; Zawada, K.; Bukowska, J. Electrochemical and Surface-Enhanced Raman Spectroscopy Studies of 4-Phenylpyridine Adsorption at the Gold/Solution Interface. *Electrochim. Acta* **2002**, *47*, 2429–2434.
36. Stoumpos, C. C.; Malliakas, C. D.; Kanatzidis, M. G. Semiconducting Tin and Lead Iodide Perovskites with Organic Cations: Phase Transitions, High Mobilities, and Near-Infrared Photoluminescent Properties. *Inorg. Chem.* **2013**, *15*, 9019–9038.
37. O' Regan, B. C.; Lenzmann, F. Charge Transport and Recombination in a Nanoscale Interpenetrating Network of n-Type and p-Type Semiconductors: Transient Photocurrent and Photovoltage Studies of TiO_2/Dye/CuSCN Photovoltaic Cells. *J. Phys. Chem. B* **2004**, *108*, 4342–4350.
38. O'Regan, B. C.; Bakker, K.; Kroeze, J.; Smit, H.; Sommeling, P.; Durrant, J. R. Measuring Charge Transport from Transient Photovoltage Rise Times. A New Tool To Investigate Electron Transport in Nanoparticle Films. *J. Phys. Chem. B* **2006**, *110*, 17155–17160.